Field-induced phase transitions and quantum criticality in the honeycomb antiferromagnet $Na_3Co_2SbO_6$

Ze Hu,[1,*] Yue Chen,[2,*] Yi Cui,[1,3] Shuo Li,[1] Cong Li,[1] Xiaoyu Xu,[1] Ying Chen,[1] Xintong Li,[2] Yuchen Gu,[2] Rong Yu,[1,3] Rui Zhou,[4] Yuan Li,[2,†] and Weiqiang Yu[1,3,‡]

[1]*Department of Physics and Beijing Key Laboratory of Opto-Electronic Functional Materials & Micro-Nano Devices, Renmin University of China, Beijing, 100872, China*

[2]*International Center for Quantum Materials, School of Physics, Peking University, Beijing 100871, China*

[3]*Key Laboratory of Quantum State Construction and Manipulation (Ministry of Education), Renmin University of China, Beijing, 100872, China*

[4]*Beijing National Laboratory for Condensed Matter Physics and Institute of Physics, Chinese Academy of Sciences, Beijing, 100190, China*

(Received 24 September 2023; revised 21 January 2024; accepted 22 January 2024; published 9 February 2024)

We performed ^{23}Na NMR measurements on a single-domain crystal of the Kitaev material $Na_3Co_2SbO_6$ with magnetic field applied along the crystalline a axis. A positive Curie-Weiss constant is obtained from the NMR Knight shift, which suggests the existence of ferromagnetic exchange couplings. The antiferromagnetic ordering is found to be suppressed at a field of 1.9 T. Inside the ordered phase, our data reveal two additional phase transitions. At 1.9 T the spin-lattice relaxation rate $1/^{23}T_1$ establishes a quantum critical behavior at high temperatures. However, at low temperatures a gapped behavior is observed at the "critical" field, which suggests a weak first-order transition instead and a possible field-induced quantum spin liquid. Our results reveal complex microscopic interactions in the system that may help to search for possible quantum spin liquids.

DOI: 10.1103/PhysRevB.109.054411

I. INTRODUCTION

The experimental search for quantum spin liquids (QSLs), representing a disordered phase beyond Landau's paradigm, containing novel properties such as fractional excitations and long-range entanglement, and promising for unconventional superconductivity and quantum computation, has been a heated frontier in condensed-matter physics [1–5]. In antiferromagnetic (AFM) systems with triangular, kagome, and pyrochlore lattice structures, strong geometric frustration may be sufficient to suppress magnetic ordering and lead to QSLs. However, it is highly debated if QSLs are established in real materials, because site or antisite disorder, which strongly affects the nature of the ground states, has been frequently reported [6–8].

In parallel, the Kitaev model in the honeycomb lattice, which contains exchange frustration among neighboring bonds with orthogonal Ising-type couplings, is a rare two-dimensional (2D) case where the QSL is an exact ground state with Majorana and photonic gauge excitations [9–11]. Theoretical studies also predict that the AFM Kitaev model carries either a Z_2 or U(1) gauge field [12–14], whereas a ferromagnetic (FM) Kitaev model only hosts Z_2 type. Until recently, it is proposed that some 4d or 5d transition-metal ions with hexagonal lattice structures, such as A_2IrO_3 (A = Li, Na) [15–18] and α-$RuCl_3$ [19–29], may contain Kitaev interactions arising from strong spin-orbit coupling and bond symmetries [30,31]. To be more interesting, hexagonal cobaltates such as $Na_2Co_2TeO_6$, $Na_3Co_2SbO_6$, and $BaCo_2(AsO_4)_2$ are proposed to be a 3d transition-metal class of QSL candidate materials, due to interplay among trigonal crystal field, charge transfer, spin-orbit coupling, and Coulomb interactions [32–37].

However, in all of these Kitaev materials, AFM ground states are usually observed [38–45]. It is then proposed that these systems should be described by a combined H-K-Γ model, where H stands for isotropic Heisenberg, K for Kitaev, and Γ for off-diagonal spin couplings, and QSL may only survive in narrow, barely reachable parameter spaces [11,46–48].

$Na_3Co_2SbO_6$, as shown in Fig. 1(a), contains edge-shared CoO_6 octahedra. Co^{2+} ions, with effective spin-1/2, form a layered honeycomb lattice, with SbO_6 octahedra located at the center in the same layer. The exchange couplings among Co^{2+} are bridged by both edge-shared oxygen (through p orbitals) and Sb (through d orbitals) atoms. Dominate FM Kitaev interactions have been proposed theoretically [34] but are yet to be proved experimentally. At zero field, the compound is ordered below $T_N \approx 6.6$ K [49], with an AFM pattern and a propagation vector $K = (1/2, 1/2, 0)$ [39,40]. The magnetic structure of $Na_3Co_2SbO_6$, as well as $Na_2Co_2TeO_6$, may not follow the simple zigzag pattern [50–53] and varies with magnetic field [44,49]. Magnetic excitations in $Na_3Co_2SbO_6$, measured by inelastic neutron scattering (INS), μSR, and NMR measurements, reveal strong quantum fluctuations and possible coexistence of H, K, and Γ exchange couplings [54–59]. However, an easy-plane XXZ model is also suggested by a

*These authors contributed equally to this study.
†yuan.li@pku.edu.cn
‡wqyu_phy@ruc.edu.cn

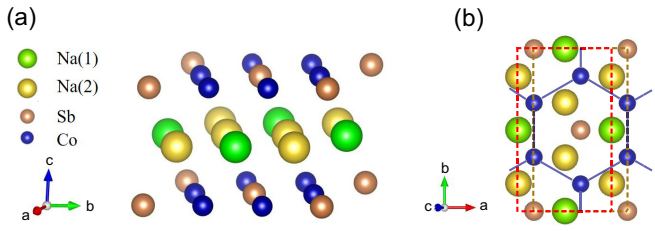

FIG. 1. Lattice structure of $Na_3Co_2SbO_6$. (a) Side view of one unit cell of the compound, where magnetic Co^{2+} ions form the layered regular honeycomb lattice, with Sb^{5+} ions located at the center of each hexagon. Oxygen atoms in the edge-shared CoO_6 octahedra are omitted for simplicity. Na^+ ions separate the magnetic layers with two types of inequivalent sites, labeled Na(1) and Na(2). (b) Top view of one half of unit cell along the c axis. The red and brown dotted lines depict the in-plane boundary that contains Na^+ and Co^{2+} ions, respectively. Na(1) and Na(2) differ slightly by their distances to neighboring Co-Co bonds.

recent study [53]. To further address these issues and search for QSL, more spectroscopic studies through tuning are highly desired [25,60,61].

In this work we report ^{23}Na NMR studies on a high-quality, twin-free single crystal of $Na_3Co_2SbO_6$. We identify a positive Curie-Weiss constant from the NMR Knight shift in the paramagnetic (PM) phase. The magnetic orderings are confirmed by the NMR spectra, and the transition temperatures are resolved by the NMR spin-lattice relaxation rates $1/^{23}T_1$. With field applied along the crystalline a axis, two additional magnetic phase transitions are found in the ordered phase, as shown by the detailed phase diagram (see Fig. 8).

Low-energy spin dynamics, revealed by the spin-lattice relaxation rates $1/^{23}T_1$, demonstrates a field suppression of magnetic order. In particular, a funnel shape in the color map of $1/^{23}T_1T$ is established at a field of 1.9 T, which is clear evidence for quantum criticality in the paramagnetic phase. However, the low temperature $1/^{23}T_1$ reveals a possible weakly first-order quantum phase transition at 1.9 T and a possible QSL at higher fields. Our study reveals the complexity of phases and magnetic exchange couplings in the system and promotes further investigations on field-induced phases, such as QSLs.

II. MATERIALS AND TECHNIQUES

High-quality single crystals were grown by the chemical vapor transport method [45]. A single-domain (twin-free) sample was selected for the current study. The usage of single-domain crystal allows one to induce a single magnetic phase with one field orientation, which also simplifies the NMR spectra. A recent low-temperature magnetization study revealed complicated phase transitions with different in-plane field orientation [49]. In this study the field is applied along the crystalline a axis, which results in a larger critical field [49] and benefits NMR measurements. The magnetic field is calibrated by the ^{63}Cu resonance frequency from the NMR tank coil.

A top tuning circuit was used to cover a wide frequency range with fields from 1 to 10 T. The ^{23}Na NMR spectra were collected by the standard spin-echo technique. For verification we also performed dc magnetization measurements at selected temperatures in a magnetic property measurement system (MPMS) with the same field orientation.

^{23}Na is an isotope with spin $I = 3/2$ and Zeeman factor $^{23}\gamma = 11.262$ MHz/T. The NMR Knight shift $^{23}K_n$ is calculated by $K_n = (f - \gamma H)/\gamma H$, where f is the peak frequency of the center NMR lines. The NMR spin-lattice relaxation rate $1/^{23}T_1$ is obtained by the inversion-recovery method, with the spin recovery curve fitted to the exponential function for spin-3/2 nuclei, $I(t) = a - b[e^{-(t/T_1)^\beta} + 9e^{-(6t/T_1)^\beta}]$, where β is the stretching factor.

III. NMR SPECTRA

In order to investigate local magnetic properties, the NMR spectra were collected at various magnetic fields and temperatures, with frequencies relative to $^{23}\gamma H$, as depicted in Figs. 2(a)–2(c). At $T = 20$ K, six ^{23}Na NMR lines are identified that correspond to two types of interlayer Na atoms, Na(1) and Na(2), as shown in Fig. 1(b), and each has one center peak and two satellite peaks. With an occupancy ratio of $N_1 : N_2 = 1 : 2$ in the lattice, where N_1 and N_2 are the number of atoms of Na(1) and Na(2), respectively, their spectra are resolved accordingly with the spectral weight of $I_1 : I_2 = N_1 : N_2 = 1 : 2$. The NMR satellites are located at about 0.83 MHz (0.52 MHz) for Na(1) [Na(2)] away from the center transition.

Upon cooling from 20 to 8 K, all peaks move toward high frequencies, as shown in Fig. 2(a), which indicates an increase of the Knight shift K_n in the PM phase, with a positive hyperfine coupling constant among ^{23}Na and Co^{2+}. At even lower temperatures, the NMR spectra broaden significantly, for example, below 6 K at 1 T [Fig. 2(a)] and below 5 K at 1.8 T [Fig. 2(b)], which clearly indicates the onset of magnetic ordering. The satellites become indistinguishable due to broadening of the spectra in the ordered phase. At low fields, with the change of local moment orientations in the lattices, the relative orientation among the ordered moments and the principle axis of the electric field gradient (EFG) also vary, resulting in additional spectral broadening in the satellites. At high fields, more NMR lines appear at low temperatures due to complicated magnetic structures, which prevents us from distinguishing the center and the satellite transitions. At a field of 2.3 T, as shown in Fig. 2(c), all peaks are resolvable again at low temperatures, consistent with the spin-polarized phase when magnetic ordering is suppressed by field [49]. Note that the integrated spectral weight, multiplied by temperature, remains as a constant at 1.9 T and above. At low fields the values drop by 30% below T_N when cooled from the PM phase to the ordered phase (data not shown). We believe that quenched disorder broadens the spectra and leads to partial loss of the signal.

To resolve the magnetic structures in the ordered phase, the spectra are displayed at a low temperature of 2 K with increasing fields, as shown in Fig. 2(d). Two broad NMR peaks are observed at 1 T, which is a direct evidence of AFM ordering. With the field increased from 1.4 to 1.6 T, more peaks are resolved, where a change of the magnetic structure is suggested. For fields above 1.9 T, six NMR peaks are seen

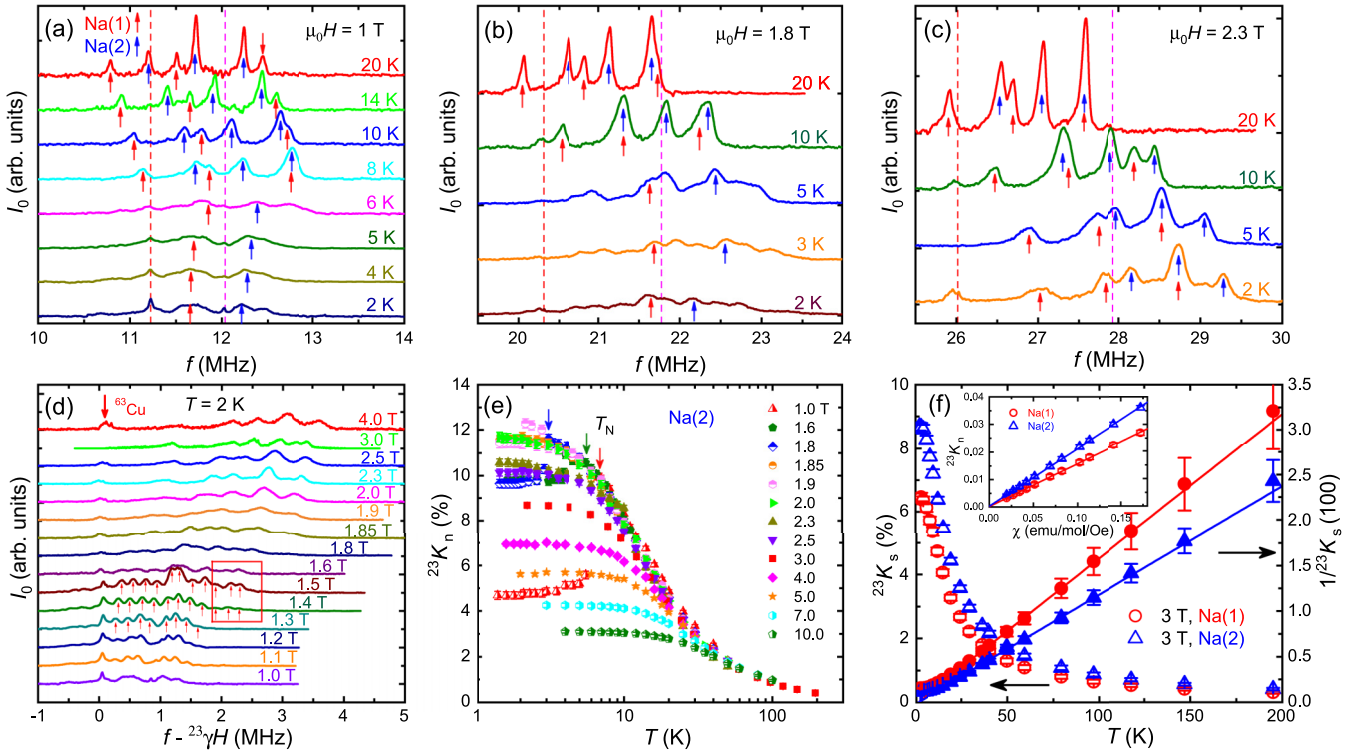

FIG. 2. NMR spectra. (a)–(c) ^{23}Na spectra measured at different temperatures with representative fields of well below (1.0 T), close to (1.8 T), and above (2.3 T) the field-induced quantum phase transition. Red and blue arrows label the Na(1) and Na(2) spectra, respectively. The orange (magenta) dashed lines denote the position of ^{63}Cu (^{65}Cu) lines from the NMR coil. (d) Full ^{23}Na NMR spectra taken at a constant temperature of 2 K with increasing fields. The red rectangle denotes emerged peaks in the AFM$\frac{1}{3}$ phase at fields of 1.4 T and above. The up-arrows mark all resolvable peaks across the phase transition. (e) Knight shift $^{23}K_n$ as a function of temperature measured at different fields. (f) Knight shift $^{23}K_s$ (left scale) and $1/^{23}K_s$ (right scale) plotted as a function of temperature, measured on both Na(1) and Na(2) at 3 T. Solid lines are linear fits to $1/^{23}K_s$ with temperature from 25 to 200 K. Inset: $^{23}K_n$ -χ plot with temperature from 25 to 200 K. Solid lines are linear fits to obtain chemical shift K_C and A_{hf}.

with overlaps of center and satellite lines of ^{23}Na from Na(1) and Na(2), where the fully polarized phase is achieved as the ground state. Therefore two magnetic phase transitions, at 1.4 and 1.9 T, respectively, are revealed.

We simulated the low-field NMR spectra with two possible magnetic structures, the zigzag order [Fig. 3(a)] [40] and the double-**q** order [Fig. 3(c)] [53], respectively. Since ^{23}Na nuclei are distant from Co^{2+} ions, only dipolar hyperfine couplings among them are taken into account. For simplicity, the NMR satellites are not considered in the simulation. The uniform magnetization of Co^{2+} by the external field would induce a rigid shift of the whole spectra but does not affect the line shape and is therefore not included in the calculations as well.

The total hyperfine field on each ^{23}Na nucleus is then obtained by summing over contributions from ordered moments of Co^{2+} with their relative coordinates. The calculated center transition lines at low field are plotted in Figs. 3(b) and 3(d), with a local moment of $0.9\,\mu_B/Co^{2+}$ assumed for the zigzag phase [40] and two local moments of $\sqrt{3}$ and 1 (in units of $0.9\,\mu_B/Co^{2+}$) in the double-**q** phase [53], respectively.

For the zigzag pattern, Na(1) produces one center line at about 0 kOe, and Na(2) produces two center lines at –0.326 kOe (–0.37 MHz) and 0.384 kOe (0.43 MHz), with a relative spectral weight of 1:1:1 [Fig. 3(b)]. By contrast, the double-**q** pattern features one center line for Na(1) at 0 kOe, and three center lines for Na(2) at –0.322 kOe (–0.36 MHz), 0 kOe,

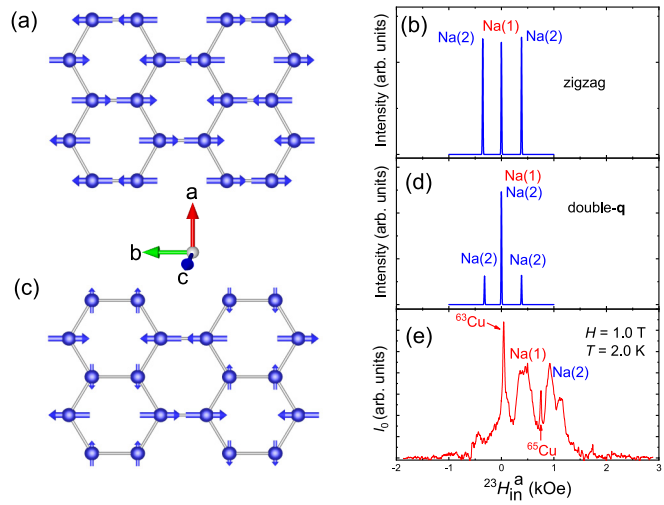

FIG. 3. Magnetic structures and simulated NMR spectra. (a), (b) Spin pattern and center ^{23}Na lines with the zigzag order (see text). (c), (d) Spin pattern and center ^{23}Na lines with the double-**q** order (see text). (e) The measured NMR spectrum at 2 K at 1 T field.

TABLE I. Curie-Weiss temperature θ obtained from different measurements with field applied along the a axis.

Measurements	$^{23}K_n$ [Na(1)]	$^{23}K_n$ [Na(2)]	M [Low T] [49]
θ (K)	1.1 ± 0.3	1.1 ± 0.3	1.0

and 0.324 kOe (0.36 MHz), which produces three lines with a relative weight of 1:4:1 [Fig. 3(d)].

The simulated three-peak spectrum with equal weights for the zigzag pattern is remarkably different from the actual spectrum, with two peaks at 1 T [Fig. 3(e)] which are assigned to be Na(1) and Na(2), respectively (see later discussion). On the other hand, for the double-**q** order, the external field may have different effects on local moments in the noncollinear structure, and the assumption of a rigid shift of spectra in the simulation may be invalid. Therefore our data do not support the zigzag order but have no obvious contradiction with the double-**q** type. We note that more distinguishable peaks emerge with fields above 1.1 T, which may suggest a very weak incommensurate component superimposed on the double-**q** pattern and smear out the detailed spectra at fields of 1 T and below.

IV. NMR KNIGHT SHIFT

The Knight shifts $^{23}K_n$ for both Na(1) and Na(2) at different fields are obtained from the resonance frequency of the center peaks. As shown in Fig. 2(e), $^{23}K_n$ for Na(2) are shown as a function of temperature. Using the relationship between Knight shift and the reported susceptibility data [49], the hyperfine interaction A_{hf} can be obtained by the slope of the $^{23}K_n - \chi$ plot, which is about 0.872 kOe/μ_B and 1.166 kOe/μ_B for Na(1) and Na(2), respectively, as shown in the inset of Fig. 2(f). Note that the orbital contribution to χ is small and has been subtracted. With this, the chemical shifts K_C, estimated by the y intercept, are $0.017\% \pm 0.005\%$ and $0.032\% \pm 0.006\%$ for Na(1) and Na(2), respectively.

The spin contribution of the Knight shift K_s is then obtained as $K_s = K_n - K_C$. In Fig. 2(f), $^{23}K_s$ of both Na(1) and Na(2) are shown at 3 T, where the rapid increase of $^{23}K_s$ upon cooling demonstrates PM behaviors. Indeed, the high-temperature data of $^{23}K_s(T)$ follow the Curie-Weiss behavior, $^{23}K_s = C/(T - \theta)$. $1/^{23}K_s$, demonstrated as a function of temperature, are well fitted by straight lines with temperatures from 200 down to 25 K. With this, the Curie-Weiss temperature is obtained as $\theta = 1.1 \pm 0.3$ K for both Na(1) and Na(2).

By comparison, the magnetic susceptibility data also reveal a positive $\theta = 1.0$ K, shown in Table I, by data fitting from 20 to 120 K with the same field orientation [49]. These small but positive Curie-Weiss temperatures obtained at high temperatures indicate that the material contains FM intralayer couplings. Given that the ground state has an AFM order [39,40], highly competing magnetic FM and AFM interactions are expected with such a small θ. Then our data support the existence of FM interactions as proposed for cobaltates with honeycomb lattices [32], although the absolute values of exchange couplings remain to be determined.

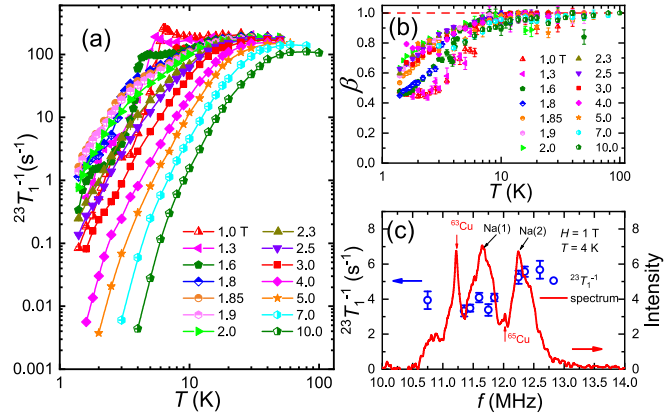

FIG. 4. Spin-lattice relaxation rates. (a) $1/^{23}T_1$ of Na(2) as a function of temperature measured under typical fields. (b) The stretching factor β as a function of temperature. (c) $1/^{23}T_1$ (left scale) measured on different frequencies of the spectrum (right scale).

V. SPIN-LATTICE RELAXATION RATES AND MAGNETIC TRANSITIONS

$1/^{23}T_1$ was measured to determine the low-energy spin fluctuations. $1/T_1$ measures the low-energy spin dynamics with $1/T_1 = T\Sigma_q A_{hf}^2(q)\frac{Im\chi(q,\omega)}{\omega}$, where $A_{hf}(q)$ is the hyperfine coupling constant, χ is the dynamic susceptibility of electrons, q is the wave vector, and ω is the NMR frequency. $1/^{23}T_1$ was measured at various frequencies across the spectra line at 4 K and 1 T, as shown in Fig. 4(c). $1/^{23}T_1$ on the right peak is about 50% larger than that on the left peak, which supports assignment of the right peak to Na(2), because Na(2) has a stronger hyperfine coupling as revealed before.

Here we primarily report $1/^{23}T_1$ measured on the center peak of Na(2). As shown in Fig. 4(a), $1/^{23}T_1$ is displayed as a function of temperature, with fields from 1 up to 10 T. The stretching factor $\beta \approx 1$ [Fig. 4(b)] in the PM phase indicates the high quality of the sample. Upon cooling, a rapid decrease of β is seen in the ordered phase and also in the fully polarized phases, which coincides with the spectral broadening at low temperatures [Figs. 2(a)–2(c)]. We think that the spectral broadening and decrease of β are caused by quenched disorder, which is very effective in the ordered phase and fully polarized phase when the local moments are large.

At low fields $1/^{23}T_1$ increases slightly upon cooling through 100 K before entering the ordered phase, which evidences the onset of low-energy spin fluctuations. In the following, three types of magnetic transitions are revealed.

First, the spin-lattice relaxation rate divided by temperature, as shown in Fig. 5, reveals all the Néel transitions at low fields, characterized by a peaked feature in $1/^{23}T_1T$ at T_N. T_N is about 6.3 K at 1 T and is barely resolvable at about 3.5 K with field at 1.8 T, below which $1/^{23}T_1T$ drops sharply with a gapped behavior. With fields from 1.85 to 1.9 T, the peaked behavior in the $1/^{23}T_1T$ is not resolvable, and the phase boundary will be determined later by a field-sweep measurement on $1/^{23}T_1T$. At 2 T and above, $1/^{23}T_1T$ exhibits a smooth decrease with temperature, which indicates the suppression of the AFM ordering. The detailed

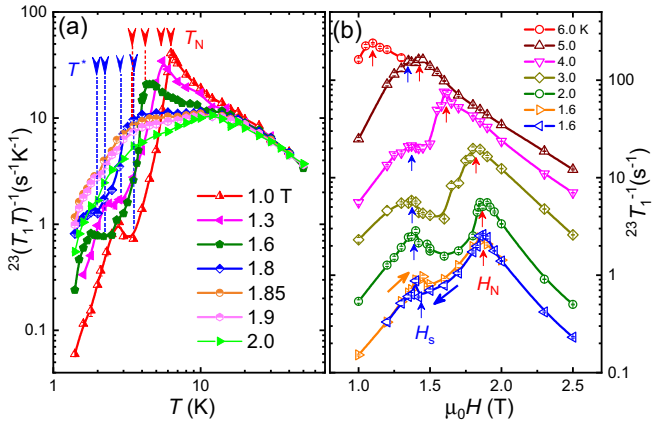

FIG. 5. Determination of magnetic phase transitions. (a) $1/^{23}T_1T$ as a function of temperature at low fields. Red and blue arrows mark the peak and "knee"-like feature in the data, denoting the double transition temperatures of T_N and T^*, respectively. (b) $1/^{23}T_1$ as a function of field under constant temperatures from 1.6 to 6 K. Up arrows denote the fields of two magnetic transitions occurring at H_N and H_s, respectively. Left and right arrows at 1.6 K illustrate the field ramping directions, where magnetic hysteresis is seen at about H_s with opposite ramping directions.

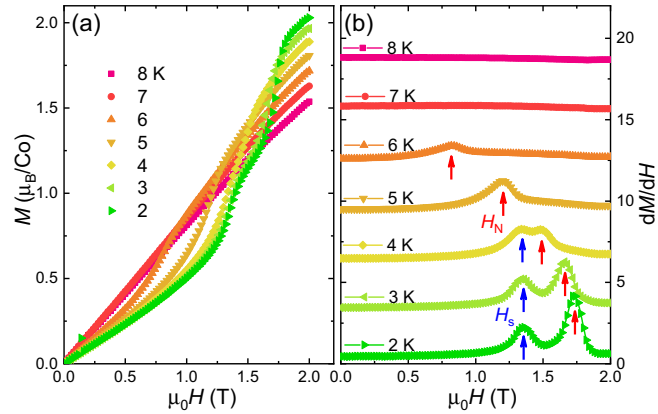

FIG. 6. Magnetization data of the sample. (a) $M(H)$ as a function of field measured at selected temperatures. (b) Calculated $dM(H)/dH$ at different temperatures. Red and blue arrows mark the peak positions of the data, labeled as H_N and H_s, respectively. Data are shifted vertically for clarity.

T_N at different fields are then added in the phase diagram (Fig. 8). The suppression of T_N is consistent with earlier susceptibility measurements [39,40]; however, our values of T_N are slightly higher, which is probably caused either by a shorter timescale of T_1 measurements or a small difference in the field alignment.

Second, with fields from 1 to 1.8 T, a "knee"-like feature is seen in $1/^{23}T_1T$ at temperatures far below T_N [Fig. 5(a)], with the onset temperatures marked as T^*. This "knee"-like behavior, rather than a continuous gapped behavior below T_N as expected with an in-plane field, reveals the emergence of additional enhanced low-energy spin fluctuations. T^* at different fields are then determined and shown in Fig. 8, which is about 3.5 K at 1 T, decreases to 2 K at 1.8 T, and diminishes at about 1.85 T. Therefore, T^* follows the same trend as T_N with field. By this we think that a weak spin reorientation may occur in the ordered phase [52]. However, such a transition is not seen in the spectra, which may be masked by the broad spectra if the change of the magnetic structure is not large.

Third, $1/^{23}T_1$, measured as a function of field at 6 K and below, demonstrates a double-peak feature with field, as shown in Fig. 5(b). The field values of the peak position in $1/^{23}T_1$ are labeled as H_N and H_s, respectively. Each H_N with the corresponding temperature is consistent with T_N measured at the same field, which therefore represents the Néel ordering as discussed before. At 1.6 K, $H_N \approx 1.87$ T; by extrapolation, the "critical" field $H_C \approx 1.9$ T at zero temperature.

On the other hand, H_s remains at a constant field of ~1.4 T but always lower than H_N. At 1.6 K a hysteresis behavior close to H_s is also revealed by the data difference with opposite field ramping directions as marked in Fig. 5(b), where H_s tends to be lower with the field ramped down. Far above or below H_s, the hysteresis behavior diminishes. This low-field peak and its hysteresis should indicate an additional first-order magnetic transition.

Such a transition at a constant field is further verified by our dc magnetization measurements. As shown in Fig. 6(a), the low-temperature magnetization $M(H)$ data are shown with field up to 2 T at selected temperatures from 8 K down to 2 K. At 2 K double magnetic transitions are clearly seen by the change of the slop in $M(H)$. For accuracy, the derivative dM/dH is then calculated and plotted in Fig. 6(b). At temperatures of 2, 3, and 4 K, dM/dH clearly shows the double-peak feature with fields also labeled as H_N and H_s, respectively. Again, H_s remains at about 1.4 T and barely changes with temperature.

For comparison, the H_N and H_s determined by $1/^{23}T_1$ and by dM/dH at each temperature are added in the phase diagram in Fig. 8. It is clearly seen that both measurements are consistent. The small difference in the field values extracted from the measurements may be due to field-calibration errors

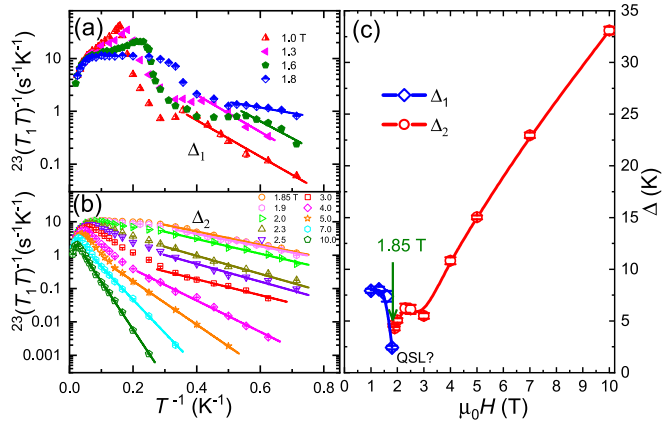

FIG. 7. Low-temperature spin gaps. (a), (b) The semilog plots of $1/^{23}T_1T$ as a function of $1/T$, below and above the "critical" field (see text), respectively. The straight lines are linear fits to data in the low-temperature regime, which determine the gaps Δ_1 and Δ_2 as labeled. (c) Δ_1 (in the ordered phase) and Δ_2 (in the disordered phase) as a function of field. Solid lines are guides to the eyes. The down arrow marks the transition field at about 1.85 T.

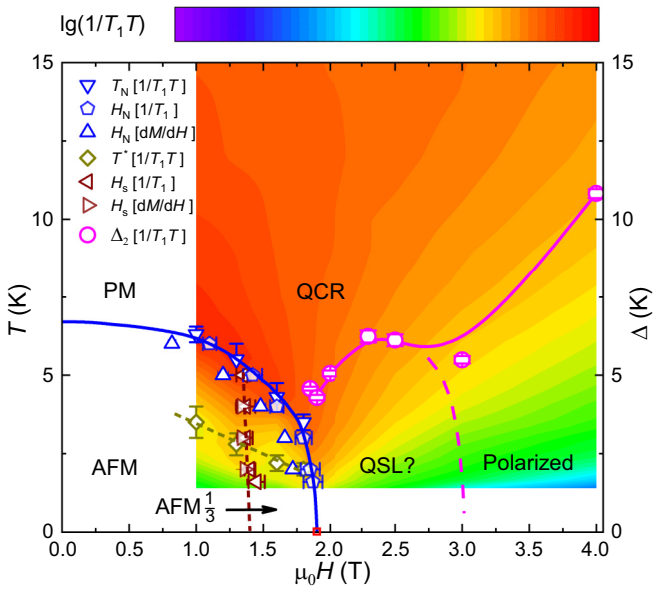

FIG. 8. Phase diagram. Colored map represents the contour plot of $1/^{23}T_1T$ data, with a QCR at high temperatures. T_N, H_N, T^*, H_s, and H_C are phase boundaries (see text) determined by different measurements as labeled. Δ_2 is the high-field spin gap. Lines are guides to the eyes.

and/or a small tilting of the field towards the "harder" a axis in the $1/^{23}T_1$ measurement. In fact, the transition at H_s is consistent with the reported first-order phase transition from an AFM ordering to a "AFM$\frac{1}{3}$" ordering, resolved by the neutron diffraction [49,53]. The AFM wave vectors switch from $(\pm a^*/2, \pm b^*/2, 0)$ to $(\pm a^*/3, \pm b^*/3, \pm c^*/3)$ through the transition, where the magnetic cell is enlarged.

VI. SPIN GAPS CLOSE TO THE CRITICAL FIELD

In principle, a quantum disordered phase is expected for fields above H_C, where the spin gap increases monotonically. However, as we show below, the low-temperature spin gap may exhibit a nonmonotonic field dependence in this region, which suggests an additional phase.

$1/^{23}T_1$ exhibits a downturn behavior at low temperatures, which suggests the onset of a spin gap both in the low-field ordered phase and the high-field spin-polarized phase, by which we fit $1/^{23}T_1T$ to an empirical function, $1/T_1T \propto e^{-\Delta/T}$. In the ordered AFM phase, $1/^{23}T_1T$ is a function of $1/T$, as shown by the semilog plots in Fig. 7(a), following straight lines in the low-temperature regime. Then the gaps, defined as Δ_1, are obtained by the linear fit and shown in Fig. 7(c) at different fields. The onset of the gapped behavior in the ordered phase, rather than a power-law temperature dependence of $1/T_1(T)$, suggests an ordering with local moments at least partially along the a axis, where a gap opens due to longitudinal fields. Similarly, above H_C a gapped behavior is also followed as shown in Fig. 7(b), and the obtained gap values, Δ_2, are also added in Fig. 7(c).

Interestingly, the gap does not drop to zero at the boundary of the ordered phase and the disordered phase. Δ_1 decreases with field and Δ_2 increases with field. They cross at fields between 1.8 and 1.9 T; however, none of them reach zero from fields between 1.8 and 1.9 T. The presence of a gap is also directly demonstrated by the sharp downturns in the log-log plot of $1/^{23}T_1T$ in all of the fields, as shown in Fig. 5(a). The absence of gapless excitations rule out a quantum critical point in the current system; instead, a weakly first-order quantum phase transition is suggested with the onset of a small gap at the transition field.

Furthermore, Δ_2 demonstrates a nonmonotonic field dependence as shown in Fig. 7(c): it increases first with field and then decreases; above 3 T, a large increase emerges again, as expected for a fully polarized phase. With fields from 1.85 to 3 T, a domelike behavior is observed. Such a domelike shape of Δ_2 strongly supports the existence of an additional phase between the AFM phase and the fully polarized phase.

VII. QUANTUM CRITICALITY AND PHASE DIAGRAM

A colored contour plot of $1/^{23}T_1T$ is shown in Fig. 8 as a function of (H, T). $1/^{23}T_1T$ is maximized when the temperature is close to T_N, which is a typical feature for a renormalized classical regime. Below 2 K, $1/^{23}T_1T$ is maximized at $H_C \approx 1.9$ T, which is a signature of a quantum phase transition with strong quantum fluctuations. At high temperatures a quantum critical region (QCR), as noted in Fig. 8, is also seen as a funnel shape in the color map, when it is getting close to 1.9 T.

With detailed data analysis performed in Sec. V, a complete magnetic phase diagram is established as shown in Fig. 8, where the PM, AFM, AFM$\frac{1}{3}$, disordered phases and their phase boundaries are determined. The gap in the disordered phase, Δ_2, is also added in the phase diagram. A QSL region is speculated just between the ordered phase and the fully polarized phase, where Δ_2 exhibits a domelike shape with field.

We also compared our results with a previous NMR work on polycrystals, where the AFM phase, the potential QSL phase, and the fully polarized phase are also proposed [59]. The usage of a single-domain single crystal allows us to resolve all the phase boundaries precisely. In addition, we identified a possible spin reorientation transition below T_N and a first-order phase transition at 1.4 T. The reported $1/^{23}T_1(T)$ of polycrystals exhibits a two-gap feature in a large field range [59] which is absent in our work and therefore should be attributed to the magnetic anisotropy of the material.

VIII. DISCUSSION

The complicated phase diagram indicates more competing exchange interactions in this system, which needs to be further studied by different probes. In particular, the nature of the transition at T^* remains unknown and needs to be verified by other measurements. One candidate mechanism for the transition is the Dzyaloshinskii-Moriya (DM) interaction, which could be effective far below T_N. Given that the inversion symmetry is broken among next-nearest neighboring Co^{2+} ions in the honeycomb lattice, a weak DM interaction is possible [62]. Because NMR is very sensitive to the low-energy spin fluctuations, such weak DM interaction may lead to the observations

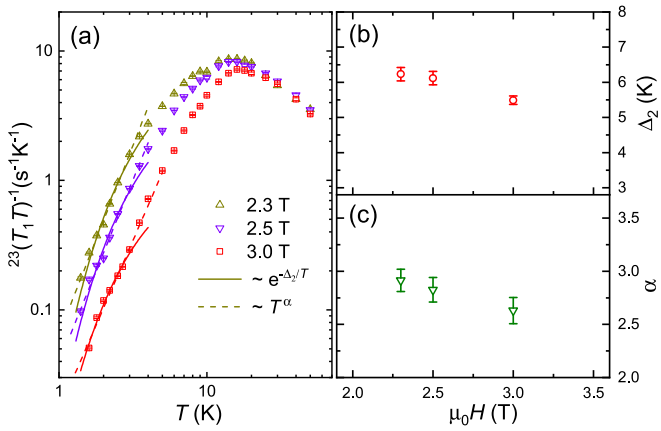

FIG. 9. Comparison of gap and power-law fits to $1/^{23}T_1T$. (a) $1/^{23}T_1T$ as a function of temperature at 2.3, 2.5, and 3.0 T. The solid lines and dashed lines represent the fit to the gapped function and the power-law function below 3 K, respectively. (b) Δ_2 as a function of field. (c) Power-law exponent α as a function of field.

below T^*. However, we are cautious that DM interaction has not been reported by other studies [39,40].

Theoretically, a first-order phase transition may occur if a QSL exists between the ordered phase and the spin-polarized phase [63–65]. We speculate that Kitaev couplings (K term) and off-diagonal (Γ term) may exist and strongly affect the spin dynamics in the system [46,66]. For comparison, in two other Kitaev materials, α-$RuCl_3$ and $Na_2Co_2TeO_6$, a new phase seems to be established between the ordered phase and the polarized phase under an in-plane magnetic field, where a QSL has been suggested [25,55,67]. A gapless behavior is observed in the low-temperature $1/T_1$ data of α-$RuCl_3$, which supports a proximate Kitaev QSL [25]. For the current compounds we think that a QSL may also exist, given the existence of a dome-shape of Δ_2.

However, we found that a power-law fitting is also applicable to the low-temperature data $1/^{23}T_1T$ with field just above H_C. As shown in Fig. 9(a), a function fit to either a gapped behavior and a power-law behavior in the same temperature range is performed at temperatures below 3 K, with fields from 2.3 to 3 T. The obtained gap Δ_2 and the power-law exponent α are depicted in Figs. 9(b) and 9(c), respectively, as a function of field. Notably, both Δ_2 and α decrease with increasing field, contradicting the expected increase of both quantities with field in the fully polarized phase. Such anomalous behavior may support a QSL interval between the ordered phase and the fully polarized phase, although we cannot differentiate a gapped or a gapless behavior with current data.

IX. SUMMARY

In summary, we investigated the static and low-energy dynamical behavior through NMR experiments on a high-quality $Na_3Co_2SbO_6$ single crystal. With field applied along the a axis, our data reveal a positive Curie-Weiss constant at high temperatures, which supports the existence of FM exchange couplings. Given the absence of FM ordering, such a FM coupling may not be the Heisenberg type. The observation of three separate transition lines with field, including T_N, T^*, and H_s, further suggests complex magnetic exchange couplings in the system, which may help to establish QSLs. Indeed, despite our observation of a QCR at high temperatures, the low-temperature gap in the magnetically disordered phase shows a nonmonotonic field dependence, which may be a signature of QSL. We hope that inelastic neutron scattering may help to address this by looking for an excitation continuum.

ACKNOWLEDGMENTS

The authors thank Z. Liu, Z. Xie, J. Ma, and Y. Wan for helpful discussions. A portion of this work was carried out at the Synergetic Extreme Condition User Facility (SECUF). This work is supported by the National Key R&D Program of China (Grants No. 2023YFA1406500, No. 2022YFA1402700, and No. 2021YFA1401900) and the National Natural Science Foundation of China (Grants No. 12134020, No. 12374156, No. 12061131004, and No. 11974405).

[1] P. W. Anderson, Resonating valence bonds: A new kind of insulator? Mater. Res. Bull. **8**, 153 (1973).
[2] L. Balents, Spin liquids in frustrated magnets, Nature (London) **464**, 199 (2010).
[3] P. W. Anderson, The resonating valence bond state in La_2CuO_4 and superconductivity, Science **235**, 1196 (1987).
[4] A. Y. Kitaev, Fault-tolerant quantum computation by anyons, Ann. Phys. **303**, 2 (2003).
[5] C. Nayak, S. H. Simon, A. Stern, M. Freedman, and S. Das Sarma, Non-Abelian anyons and topological quantum computation, Rev. Mod. Phys. **80**, 1083 (2008).
[6] Y. Shimizu, K. Miyagawa, K. Kanoda, M. Maesato, and G. Saito, Spin liquid state in an organic Mott insulator with a triangular lattice, Phys. Rev. Lett. **91**, 107001 (2003).
[7] T.-H. Han, J. S. Helton, S. Chu, D. G. Nocera, J. A. Rodriguez-Rivera, C. Broholm, and Y. S. Lee, Fractionalized excitations in the spin-liquid state of a kagome-lattice antiferromagnet, Nature (London) **492**, 406 (2012).
[8] J. S. Gardner, M. J. P. Gingras, and J. E. Greedan, Magnetic pyrochlore oxides, Rev. Mod. Phys. **82**, 53 (2010).
[9] A. Kitaev, Anyons in an exactly solved model and beyond, Ann. Phys. **321**, 2 (2006).
[10] Y. Motome and J. Nasu, Hunting Majorana fermions in Kitaev magnets, J. Phys. Soc. Jpn. **89**, 012002 (2020).
[11] H. Takagi, T. Takayama, G. Jackeli, G. Khaliullin, and S. E. Nagler, Concept and realization of Kitaev quantum spin liquids, Nat. Rev. Phys. **1**, 264 (2019).
[12] C. Hickey and S. Trebst, Emergence of a field-driven U(1) spin liquid in the Kitaev honeycomb model, Nat. Commun. **10**, 530 (2019).
[13] C. Hickey, C. Berke, P. P. Stavropoulos, H.-Y. Kee, and S. Trebst, Field-driven gapless spin liquid in the spin-1

Kitaev honeycomb model, Phys. Rev. Res. **2**, 023361 (2020).

[14] D. A. S. Kaib, S. M. Winter, and R. Valentí, Kitaev honeycomb models in magnetic fields: Dynamical response and dual models, Phys. Rev. B **100**, 144445 (2019).

[15] S. K. Choi, R. Coldea, A. N. Kolmogorov, T. Lancaster, I. I. Mazin, S. J. Blundell, P. G. Radaelli, Y. Singh, P. Gegenwart, K. R. Choi, S.-W. Cheong, P. J. Baker, C. Stock, and J. Taylor, Spin waves and revised crystal structure of honeycomb iridate Na_2IrO_3, Phys. Rev. Lett. **108**, 127204 (2012).

[16] S. H. Chun, J.-W. Kim, J. Kim, H. Zheng, C. C. Stoumpos, C. D. Malliakas, J. F. Mitchell, K. Mehlawat, Y. Singh, Y. Choi, Y. Gog, A. Al-Zein, M. M. Sala, M. Krisch, J. Chaloupka, G. Jackeli, G. Khaliullin, and B. J. Kim, Direct evidence for dominant bond-directional interactions in a honeycomb lattice iridate Na_2IrO_3, Nat. Phys. **11**, 462 (2015).

[17] I. Kimchi and Y.-Z. You, Kitaev-Heisenberg-J_2-J_3 model for the iridates A_2IrO_3, Phys. Rev. B **84**, 180407(R) (2011).

[18] J. Kim, J. Chaloupka, Y. Singh, J. W. Kim, B. J. Kim, D. Casa, A. Said, X. Huang, and T. Gog, Dynamic spin correlations in the honeycomb lattice Na_2IrO_3 measured by resonant inelastic x-ray scattering, Phys. Rev. X **10**, 021034 (2020).

[19] K. W. Plumb, J. P. Clancy, L. J. Sandilands, V. V. Shankar, Y. F. Hu, K. S. Burch, H.-Y. Kee, and Y.-J. Kim, $\alpha - RuCl_3$: A spin-orbit assisted Mott insulator on a honeycomb lattice, Phys. Rev. B **90**, 041112(R) (2014).

[20] Y. Kubota, H. Tanaka, T. Ono, Y. Narumi, and K. Kindo, Successive magnetic phase transitions in $\alpha - RuCl_3$: XY-like frustrated magnet on the honeycomb lattice, Phys. Rev. B **91**, 094422 (2015).

[21] S.-H. Baek, S.-H. Do, K.-Y. Choi, Y. S. Kwon, A. U. B. Wolter, S. Nishimoto, J. van den Brink, and B. Büchner, Evidence for a field-induced quantum spin liquid in α-$RuCl_3$, Phys. Rev. Lett. **119**, 037201 (2017).

[22] S. H. Do, S. Y. Park, J. Yoshitake, J. Nasu, and S. Ji, Majorana fermions in the Kitaev quantum spin system α-$RuCl_3$, Nat. Phys. **13**, 1079 (2017).

[23] A. Banerjee, C. A. Bridges, J.-Q. Yan, A. A. Aczel, L. Li, M. B. Stone, G. E. Granroth, M. D. Lumsden, Y. Yiu, J. Knolle, S. Bhattacharjee, D. L. Kovrizhin, R. Moessner, D. A. Tennant, D. G. Mandrus, and S. E. Nagler, Proximate Kitaev quantum spin liquid behaviour in a honeycomb magnet, Nat. Mater. **15**, 733 (2016).

[24] A. Banerjee, J. Yan, J. Knolle, C. A. Bridges, M. B. Stone, M. D. Lumsden, D. G. Mandrus, D. A. Tennant, R. Moessner, and S. E. Nagler, Neutron scattering in the proximate quantum spin liquid α-$RuCl_3$, Science **356**, 1055 (2017).

[25] J. Zheng, K. Ran, T. Li, J. Wang, P. Wang, B. Liu, Z.-X. Liu, B. Normand, J. Wen, and W. Yu, Gapless spin excitations in the field-induced quantum spin liquid phase of α-$RuCl_3$, Phys. Rev. Lett. **119**, 227208 (2017).

[26] A. Banerjee, P. Lampen-Kelley, J. Knolle, C. Balz, A. A. Aczel, B. Winn, Y. Liu, D. Pajerowski, J. Yan, C. A. Bridges, A. T. Savici, B. C. Chakoumakos, M. D. Lumsden, D. A. Tennant, R. Moessner, D. G. Mandrus, and S. E. Nagler, Excitations in the field-induced quantum spin liquid state of α-$RuCl_3$, npj Quantum Mater. **3**, 8 (2018).

[27] J. A. Sears, L. E. Chern, S. Kim, P. J. Bereciartua, and Y. J. Kim, Ferromagnetic Kitaev interaction and the origin of large magnetic anisotropy in α-$RuCl_3$, Nat. Phys. **16**, 837 (2020).

[28] Y. Kasahara, T. Ohnishi, Y. Mizukami, O. Tanaka, S. Ma, K. Sugii, N. Kurita, H. Tanaka, J. Nasu, Y. Motome, T. Shibauchi, and Y. Matsuda, Majorana quantization and half-integer thermal quantum Hall effect in a Kitaev spin liquid, Nature (London) **559**, 227 (2018).

[29] M. Gohlke, G. Wachtel, Y. Yamaji, F. Pollmann, and Y. B. Kim, Quantum spin liquid signatures in Kitaev-like frustrated magnets, Phys. Rev. B **97**, 075126 (2018).

[30] G. Jackeli and G. Khaliullin, Mott insulators in the strong spin-orbit coupling limit: From Heisenberg to a quantum compass and Kitaev models, Phys. Rev. Lett. **102**, 017205 (2009).

[31] J. G. Rau, Eric Kin-Ho Lee, and H.-Y. Kee, Generic spin model for the honeycomb iridates beyond the Kitaev limit, Phys. Rev. Lett. **112**, 077204 (2014).

[32] H. Liu and G. Khaliullin, Pseudospin exchange interactions in d^7 cobalt compounds: Possible realization of the Kitaev model, Phys. Rev. B **97**, 014407 (2018).

[33] R. Sano, Y. Kato, and Y. Motome, Kitaev-Heisenberg Hamiltonian for high-spin d^7 Mott insulators, Phys. Rev. B **97**, 014408 (2018).

[34] H. Liu, J. Chaloupka, and G. Khaliullin, Kitaev spin liquid in $3d$ transition metal compounds, Phys. Rev. Lett. **125**, 047201 (2020).

[35] C. Kim, H. Kim, and J. Park, Spin-orbital entangled state and realization of Kitaev physics in $3d$ cobalt compounds: A progress report, J. Phys.: Condens. Matter **34**, 023001 (2021).

[36] H. Liu, Towards Kitaev spin liquid in 3D transition metal compounds, Int. J. Mod. Phys. B **35**, 2130006 (2021).

[37] A. L. Sanders, R. A. Mole, J. Liu, A. J. Brown, D. Yu, C. D. Ling, and S. Rachel, Dominant Kitaev interactions in the honeycomb materials $Na_3Co_2SbO_6$ and $Na_2Co_2TeO_6$, Phys. Rev. B **106**, 014413 (2022).

[38] A. K. Bera, S. M. Yusuf, A. Kumar, and C. Ritter, Zigzag antiferromagnetic ground state with anisotropic correlation lengths in the quasi-two-dimensional honeycomb lattice compound $Na_2Co_2TeO_6$, Phys. Rev. B **95**, 094424 (2017).

[39] C. Wong, M. Avdeev, and C. D. Ling, Zig-zag magnetic ordering in honeycomb-layered $Na_3Co_2SbO_6$, J. Solid State Chem. **243**, 18 (2016).

[40] J.-Q. Yan, S. Okamoto, Y. Wu, Q. Zheng, H. D. Zhou, H. B. Cao, and M. A. McGuire, Magnetic order in single crystals of $Na_3Co_2SbO_6$ with a honeycomb arrangement of $3d^7$ Co^{2+} ions, Phys. Rev. Mater. **3**, 074405 (2019).

[41] S. Das, S. Voleti, T. Saha-Dasgupta, and A. Paramekanti, XY magnetism, Kitaev exchange, and long-range frustration in the $J_{\text{eff}} = \frac{1}{2}$ honeycomb cobaltates, Phys. Rev. B **104**, 134425 (2021).

[42] L. Viciu, Q. Huang, E. Morosan, H. W. Zandbergen, N. I. Greenbaum, T. McQueen, and R. J. Cava, Structure and basic magnetic properties of the honeycomb lattice compounds $Na_2Co_2TeO_6$ and $Na_3Co_2SbO_6$, J. Solid State Chem. **180**, 1060 (2007).

[43] E. Lefrançois, M. Songvilay, J. Robert, G. Nataf, E. Jordan, L. Chaix, C. V. Colin, P. Lejay, A. Hadj-Azzem, R. Ballou, and V. Simonet, Magnetic properties of the honeycomb oxide $Na_3Co_2SbO_6$, Phys. Rev. B **94**, 214416 (2016).

[44] W. Yao and Y. Li, Ferrimagnetism and anisotropic phase tunability by magnetic fields in $Na_2Co_2TeO_6$, Phys. Rev. B **101**, 085120 (2020).

[45] G. Xiao, Z. Xia, W. Zhang, X. Yue, S. Huang, X. Zhang, F. Yang, Y. Song, M. Wei, H. Deng, and D. Jiang, Crystal growth and the magnetic properties of $Na_2Co_2TeO_6$ with quasi-two-dimensional honeycomb lattice, Cryst. Growth Des. **19**, 2658 (2019).

[46] Q. Luo, J. Zhao, H.-Y. Kee, and X. Wang, Gapless quantum spin liquid in a honeycomb γ magnet, npj Quantum Mater. **6**, 57 (2021).

[47] D. Gotfryd, J. Rusnačko, K. Wohlfeld, G. Jackeli, J. Chaloupka, and A. M. Oleś, Phase diagram and spin correlations of the Kitaev-Heisenberg model: Importance of quantum effects, Phys. Rev. B **95**, 024426 (2017).

[48] P. A. Maksimov, Z. Zhu, S. R. White, and A. L. Chernyshev, Anisotropic-exchange magnets on a triangular lattice: Spin waves, accidental degeneracies, and dual spin liquids, Phys. Rev. X **9**, 021017 (2019).

[49] X. Li, Y. Gu, Y. Chen, V. O. Garlea, K. Iida, K. Kamazawa, Y. Li, G. Deng, Q. Xiao, X. Zheng, Z. Ye, Y. Peng, I. A. Zaliznyak, J. M. Tranquada, and Y. Li, Giant magnetic in-plane anisotropy and competing instabilities in $Na_3Co_2SbO_6$, Phys. Rev. X **12**, 041024 (2022).

[50] W. Chen, X. Li, Z. Hu, Z. Hu, L. Yue, R. Sutarto, F. He, K. Iida, K. Kamazawa, W. Yu, X. Lin, and Y. Li, Spin-orbit phase behavior of $Na_2Co_2TeO_6$ at low temperatures, Phys. Rev. B **103**, L180404 (2021).

[51] W. Yao, Y. Zhao, Y. Qiu, C. Balz, J. R. Stewart, J. W. Lynn, and Y. Li, Magnetic ground state of the Kitaev $Na_2Co_2TeO_6$ spin liquid candidate, Phys. Rev. Res. **5**, L022045 (2023).

[52] C. H. Lee, S. Lee, Y. S. Choi, Z. H. Jang, R. Kalaivanan, R. Sankar, and K.-Y. Choi, Multistage development of anisotropic magnetic correlations in the Co-based honeycomb lattice $Na_2Co_2TeO_6$, Phys. Rev. B **103**, 214447 (2021).

[53] Y. Gu, X. Li, Y. Chen, K. Iida, A. Nakao, K. Munakata, V. O. Garlea, Y. Li, G. Deng, I. A. Zaliznyak, J. M. Tranquada, and Y. Li, Easy-plane multi-**q** magnetic ground state of $Na_3Co_2SbO_6$, arXiv:2306.07175.

[54] C. Kim, J. Jeong, G. Lin, P. Park, T. Masuda, S. Asai, S. Itoh, H.-S. Kim, H. Zhou, J. Ma, and J.-G. Park, Antiferromagnetic Kitaev interaction in $J_{\text{eff}} = 1/2$ cobalt honeycomb materials $Na_3Co_2SbO_6$ and $Na_2Co_2TeO_6$, J. Phys.: Condens. Matter **34**, 045802 (2022).

[55] G. Lin, J. Jeong, C. Kim, Y. Wang, Q. Huang, T. Masuda, S. Asai, S. Itoh, G. Günther, M. Russina, Z. Lu, J. Sheng, L. Wang, J. Wang, G. Wang, Q. Ren, C. Xi, W. Tong, L. Ling, Z. Liu *et al.*, Field-induced quantum spin disordered state in spin-1/2 honeycomb magnet $Na_2Co_2TeO_6$, Nat. Commun. **12**, 5559 (2021).

[56] M. Songvilay, J. Robert, S. Petit, J. A. Rodriguez-Rivera, W. D. Ratcliff, F. Damay, V. Balédent, M. Jiménez-Ruiz, P. Lejay, E. Pachoud, A. Hadj-Azzem, V. Simonet, and C. Stock, Kitaev interactions in the Co honeycomb antiferromagnets $Na_3Co_2SbO_6$ and $Na_2Co_2TeO_6$, Phys. Rev. B **102**, 224429 (2020).

[57] W. Yao, K. Iida, K. Kamazawa, and Y. Li, Excitations in the ordered and paramagnetic states of honeycomb magnet $Na_2Co_2TeO_6$, Phys. Rev. Lett. **129**, 147202 (2022).

[58] P. Miao, X. Jin, W. Yao, Y. Chen, A. Koda, Z. Tan, W. Xie, W. Ji, T. Kamiyama, and Y. Li, Persistent spin dynamics in magnetically ordered honeycomb cobalt oxides, arXiv:2307.16451.

[59] E. Vavilova, T. Vasilchikova, A. Vasiliev, D. Mikhailova, V. Nalbandyan, E. Zvereva, and S. V. Streltsov, Magnetic phase diagram and possible Kitaev-like behavior of the honeycomb-lattice antimonate $Na_3Co_2SbO_6$, Phys. Rev. B **107**, 054411 (2023).

[60] Y.-T. Jia, C.-S. Gong, Y.-X. Liu, J.-F. Zhao, C. Dong, G.-Y. Dai, X.-D. Li, H.-C. Lei, R.-Z. Yu, G.-M. Zhang, and C.-Q. Jin, Mott transition and superconductivity in quantum spin liquid candidate $NaYbSe_2$, Chin. Phys. Lett. **37**, 097404 (2020).

[61] Z.-X. Liu and B. Normand, Dirac and chiral quantum spin liquids on the honeycomb lattice in a magnetic field, Phys. Rev. Lett. **120**, 187201 (2018).

[62] L. Chen, J.-H. Chung, B. Gao, T. Chen, M. B. Stone, A. I. Kolesnikov, Q. Huang, and P. Dai, Topological spin excitations in honeycomb ferromagnet CrI_3, Phys. Rev. X **8**, 041028 (2018).

[63] I. Makhfudz, Fluctuation-induced first-order quantum phase transition of the $U(1)$ spin liquid in a pyrochlore quantum spin ice, Phys. Rev. B **89**, 024401 (2014).

[64] R. Schönemann, S. Imajo, F. Weickert, J. Yan, D. G. Mandrus, Y. Takano, E. L. Brosha, P. F. S. Rosa, S. E. Nagler, K. Kindo, and M. Jaime, Thermal and magnetoelastic properties of $\alpha - RuCl_3$ in the field-induced low-temperature states, Phys. Rev. B **102**, 214432 (2020).

[65] H. Tomishige, J. Nasu, and A. Koga, Interlayer coupling effect on a bilayer Kitaev model, Phys. Rev. B **97**, 094403 (2018).

[66] Q. Luo, J. Zhao, X. Wang, and H.-Y. Kee, Unveiling the phase diagram of a bond-alternating spin-$\frac{1}{2}$ K-Γ chain, Phys. Rev. B **103**, 144423 (2021).

[67] J. A. Sears, Y. Zhao, Z. Xu, J. W. Lynn, and Y.-J. Kim, Phase diagram of $\alpha - RuCl_3$ in an in-plane magnetic field, Phys. Rev. B **95**, 180411(R) (2017).